Data repository: A new kind of invisible gold in pyrite hosted in deformation-related dislocations

Denis Fougerouse[1,2], Steven M. Reddy[1,2], Mark Aylmore[2], Lin Yang[3], Paul Guagliardo[4], David W. Saxey[2], William D.A. Rickard[2], Nicholas Timms[1]

[1]School of Earth and Planetary Sciences, Curtin University, Perth, Australia

[2]Geoscience Atom Probe Facility, John de Laeter Centre, Curtin University, Perth, Australia

[3]China University of Geosciences, Beijing, China

[4]Centre for Microscopy, Characterisation and Analysis, The University of Western Australia, Crawley, Australia

1. The Huangjindong gold deposit

The Jiangnan Orogen, located in China between the Yangtze and Cathaysia Blocks (Deng and Wang 2016), contains total gold resources of ~ 970 t (Xu et al. 2017). The Orogen was formed by a collision between the Yangtze and the Cathaysia Blocks during the assembly of the Rodinia Supercontinent from the late Mesoproterozoic to early Neoproterozoic (Li et al., 2008; Li et al., 2009). After formation, it experienced Early Paleozoic intracontinental orogeny, Early Mesozoic folding and thrusting related to the formation of Qinling-Dabie orogeny, and Late Mesozoic formation of the Basin-and-Range-like topography caused by the subduction of the Paleo-Pacific Plate (Shu, 2006; Zhang et al., 2019).

The Huangjindong gold deposit with gold reserves of ~82 t and an average grade of 5 g/t is hosted by the Changsha-Pingjiang fault zone in the central part of the Jiangnan Orogen (Fig. 1b; Zhang et al., 2020). The host rocks in the Huangjindong deposit are Neoproterozoic slates that formed from regional lower- to midgreenschist-facies metamorphism of turbidites (Zhang et al., 2019). Due to lack of reliable minerals for dating, mineralization age of the Huangjindong gold deposit is uncertain, varying from 460 Ma to 150 Ma (Zhang et al., 2019).

Based on the mineral assemblage, fluid inclusions studies and arsenopyrite thermobarometry, the gold mineralization was estimated to have occurred at a depth of 5 ± 1 km and temperature of 200–350 °C (Li et al. 2011; Liu et al. 2017).

The studied sample, D02B3 (114.049008 N, 28.675227 E), is a representative gold ore from E-W-trending, 1-m-thickness orebody (dipping 45–70° S; Zhang et al., 2020), which comprises barren white quartz, auriferous grey quartz and gold-mineralized slates. The main minerals in the sample include quartz, sericite, pyrite and arsenopyrite with minor chalcopyrite, tetrahedrite, galena and native gold (Zhang et al., 2020). Gold mainly occurs as refractory gold within arsenopyrite or pyrite in the sample.

2. Methods

The electron backscattered diffraction (EBSD) analyses were performed with the TESCAN Clara field emission gun scanning electron microscope (FEG-SEM) equipped with an Oxford Instruments Symmetry EBSD detector in the John de Laeter Centre at Curtin University. The EBSD data was process with the Oxford Symmetry software. The maps are coloured using the perceptually uniform Imola colour scheme (Crameri, 2018). Within the pyrite a ~2° low-angle boundary was selected for NanoSIMS analyses.

The CAMECA NanoSIMS 50L at the Centre for Microscopy, Characterisation and Analysis at the University of Western Australia, was used in this study. Measurements were carried out with a Cs+ primary beam, with a spot size of approximately 100 nm, impact energy of 16 keV, and a beam current of 0.6 pA. Secondary ion images were obtained by rastering the primary ion beam across areas measuring 50 μm^2, at a resolution of 512 x 512 pixels, with a counting time of 15 ms per pixel.

The TESCAN Lyra3 Ga+ focused ion beam coupled SEM (FIB-SEM) in the John de Laeter Centre at Curtin University was used to prepare atom probe needle-shaped specimens. The FIB-SEM was operated at an accelerating voltage of 30kV during the extraction and shaping of the specimen and a final cleaning routine at an accelerating voltage of 2kV was used to remove the layer affected by high-energy Ga ions.

Atom probe specimens were analysed with the CAMECA LEAP 4000X HR Geoscience Atom Probe in the John de Laeter Centre at Curtin University. The specimens were analysed in laser assisted mode with a UV laser (λ = 355 nm), pulsed at 125 kHz and a laser pulse energy of 35 pJ. The specimen base temperature was maintained at 60 K and the automated detection rate at 0.01 atom/pulse. In the mass-to-charge ratio spectrum, peaks twice higher than the background were identified and ranged. The composition of the dislocation were calculating by extracting the composition of isoconcentration surfaces defined by 0.3 at.% Ni. The 1D concentration profiles were generated normal to the boundary through the dislocations with a step size of 1 nm. Additional details about the data acquisition and quality is given in table S1 following the recommendations of Blum et al 2018.

3. References

Blum, T.B., Darling, J.R., Kelly, T.F., Larson, D.J., Moser, D.E., Perez-Huerta, A., Prosa, T.J., Reddy, S.M., Reinhard, D.A., Saxey, D.W., 2018. Best practices for reporting atom probe analysis of geological materials. Microstructural Geochronology: Planetary Records Down to Atom Scale 369-373.

Crameri, F., 2018. Geodynamic diagnostics, scientific visualisation and StagLab 3.0. Geoscientific Model Development, 11(6), 2541-2562.

Deng, J., Wang, Q.F., 2016. Gold mineralization in China: metallogenic provinces, deposit types and tectonic framework. Gondwana Res. 36, 219–274.

Li, J., Chen, B.H., An, J.H., Tan, S.M., Zhang, X.G., Yao, Y.J., (2011).Characteristics of fluid inclusions of the Huangjindong gold deposit, Hunan Province. Geol Miner Resour South China 27:163–168 (in Chinese with English abstract).

Li, X.H., Li, W.X., Li, Z.X., Lo, Q.H., Wang, J., Ye, M.F., Yang, Y.H., 2009. Amalgamation between the Yangtze and Cathaysia Blocks in South China: constraints from SHRIMP U-Pb zircon ages, geochemistry and Nd-Hf isotopes of the Shuangxiwu volcanic rocks. Precambr. Res. 174, 117–128.

Li, Z.X., Bogdanova, S.V., Collins, A.S., Davidson, A., De Waele, B., Ernst, R.E., Fitzsimons, I.C.W., Fuck, R.A., Gladkochub, D.P., Jacobs, J., Karlstrom, K.E., Lu, S., Natapov, L.M., Pease, V., Pisarevsky, S.A., Thrane, K., Vernikovsky, V., 2008. Assembly, configuration, and break-up history of Rodinia: a synthesis. Precambr. Res. 160, 179–210.

Liu, Y., Zhang, L., Sun, S.C., Qi, P., Wu, S.G., Gao, L., 2017. Mineralization mechanism of Yangshanzhuang gold deposit, northeastern Hunan Province. Acta Petrol Sin 33:2273–2284 (in Chinese with English abstract)

Shu, L.S., 2006. Pre-Devonian tectonic evolution of south China from Cathaysian Block to Caledonian Period folded orogenic belt. Geol. J China Univ. 12, 418–431 (in Chinese with English abstract).

Xu, D.R., Deng, T., Chi, G.X., Wang, Z.L., Zou, F.H., Zhang, J.L., Zou, S.H., 2017. Gold mineralization in the Jiangnan orogenic belt of south China: Geological, geochemical and geochronological characteristics, ore deposit-type and geodynamic setting. Ore Geol. Rev. 88, 565–618.

Zhang, L., Groves, D.I., Yang, L.Q., Sun, S.C., Weinberg, R.F., Wang, J.Y., Wu, S.G., Gao, L., Yuan, L.L., Li, R.H., 2020. Utilization of pre-existing competent and barren quartz veins as hosts to later orogenic gold ores at Huangjindong gold deposit, Jiangnan Orogen, southern China. Mineral. Deposita 55, 363–380.

Zhang, L., Yang, L.Q., Groves, D.I., Sun, S.C., Chen, J.H., 2019. An overview of timing and structural geometry of gold, gold-antimony and antimony mineralization in the Jiangnan Orogen, southern China. Ore Geology Reviews, 115, 103173.
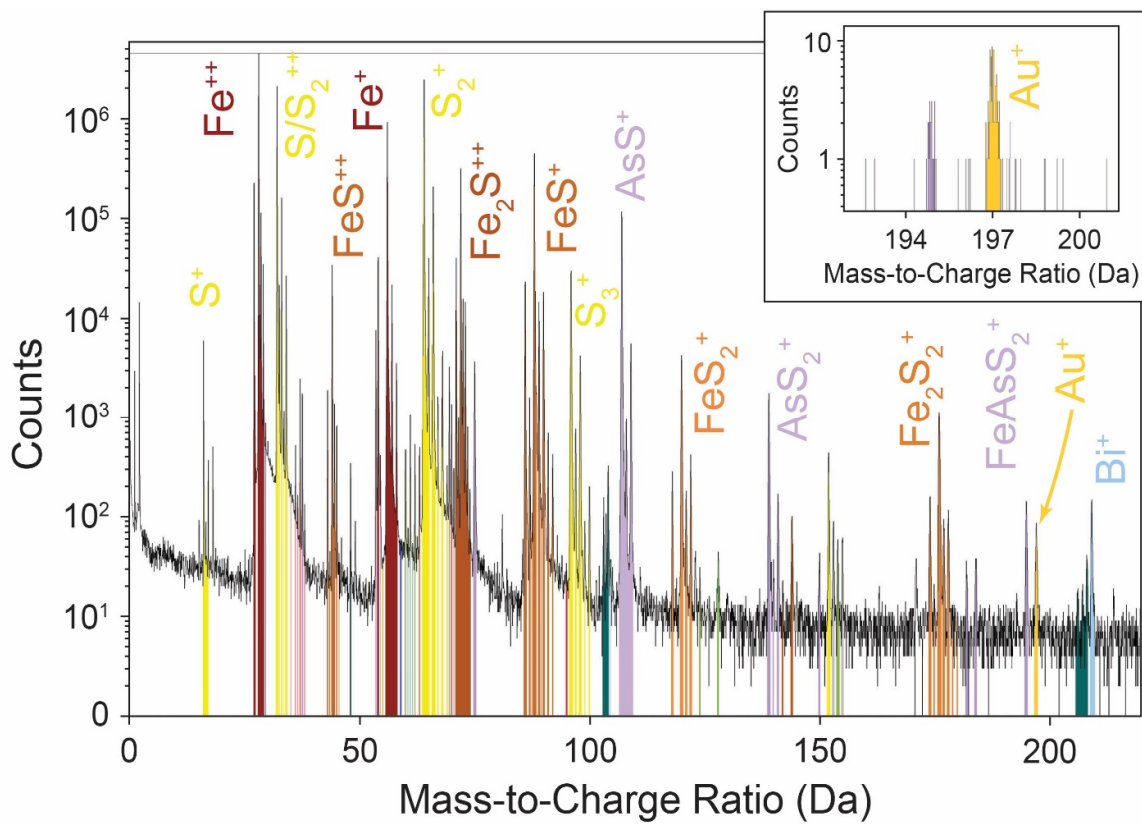
4. Figure S1

Figure S1: APT mass spectra of specimen 1. The inset is extracted from the combined dislocations as defined by an isosurface concentration of 0.3 at.% Ni.
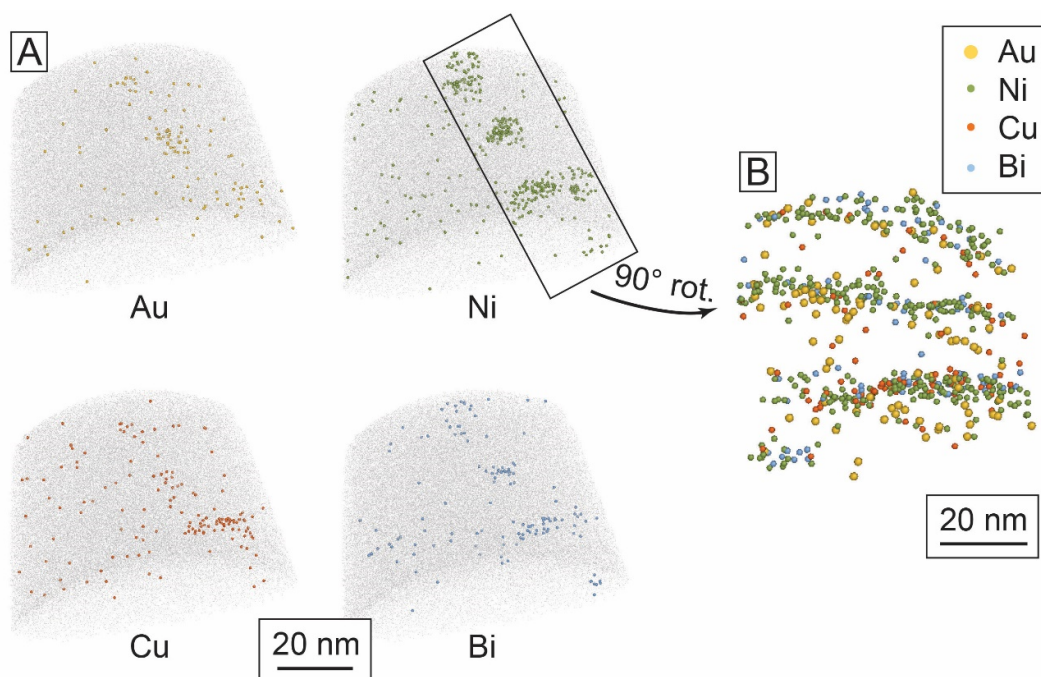
5. Figure S2

Figure S2: APT results of specimen 2. A&B) Each sphere represents an atom. The low angle boundary plane is composed of sub-horizontal gold, Ni, Cu and Bi enriched dislocations.

6. Table S1

Specimen/Data Set	Specimen 1	Specimen 2
Instrument Model	LEAP 4000X HR	LEAP 4000X HR
Instrument Settings		
Laser Wavelength (nm)	355	355
Laser Pulse Energy (pJ)	35	35
Pulse Frequency (kHz)	125	125
Evaporation Control	Detection Rate	Detection Rate
Target Detection Rate (ions/pulse)	0.01	0.01
Nominal Flight Path (mm)	382	382
Set Point Temperature (K)	60	60
Chamber Pressure (Torr)	3.20×10^{-11}	3.37×10^{-11}
Data Summary		
LAS Root Version	15.41.342i	15.41.342i
CAMECAROOT Version	18.46.492	18.46.492
Analysis Software	AP Suite 6.0	AP Suite 6.0
Total Ions:	22,497,605	4,466,850
Single	60.53%	57.28%
Multiple	38.97%	42.05%
Partial	0.50%	0.67%
Reconstructed Ions:	20,072,687	3,946,934
Ranged	89.22%	88.36%
Unranged	10.78%	11.64%
Mass Calib. (peaks/interp.)	5/Lin.	5/Lin.
[†]$(M/\Delta M)$	725	649
[††]$(M/\Delta M_{10})$	346	275
time independent background (ppm/ns)	1.7	1.8
Reconstruction		
Final specimen state	Fractured	Fractured
Pre-/Post-analysis Imaging	SEM/n.a.	SEM/n.a.
Radius Evolution Model	"voltage"	"voltage"
Field Factor (k)	3.3	3.3
Image Compression Factor	1.65	1.65
Assumed E-Field (V/nm)	19	19
Detector Efficiency	36%	36%
Avg. Atomic Volume (nm³)	0.01325	0.01325
$V_{initial}$ (V)	3320	3138

[†]ΔM is full width at half maximum.

[††]ΔM_{10} is full width at tenth maximum.

Table S1: Instrument and reconstruction parameters for APT analyses following recommendations of Blum et al. (2018).